Konya Mühendislik Bilimleri Dergisi, c. 13, s. 1, 110-131, 2025
Konya Journal of Engineering Sciences, v. 13, n. 1, 110-131, 2025
ISSN: 2667-8055 (Electronic)
DOI: 10.36306/konjes.1554353

ONE-STATION, DOUBLE-STATION AND ARRAY ANALYSIS OF RAYLEIGH SURFACE WAVES APPLIED TO A COMMON-SHOT GATHER: A PROGRAMMED TECHNIQUE DESCRIBED THROUGH SYNTHETIC SEISMOGRAMS IN NEAR-SURFACE

*** Özcan ÇAKIR**

[1] *Süleyman Demirel University, Engineering and Natural Sciences Faculty, Geophysics Department, Isparta, TÜRKİYE*
ozcancakir@sdu.edu.tr

Highlights

- Rayleigh surface waves are effective to resolve the near-surface shear-wave velocity structure
- Shear-wave velocity structure is inverted using three methods in coordination
- One-dimensional solutions are combined to build two-dimensional structure of the subsurface

***Corresponding Author:** Özcan ÇAKIR, ozcancakir@sdu.edu.tr

Konya Mühendislik Bilimleri Dergisi, c. 13, s. 1, 110-131, 2025
Konya Journal of Engineering Sciences, v. 13, n. 1, 110-131, 2025
ISSN: 2667-8055 (Electronic)
DOI: 10.36306/konjes.1554353

ONE-STATION, DOUBLE-STATION AND ARRAY ANALYSIS OF RAYLEIGH SURFACE WAVES APPLIED TO A COMMON-SHOT GATHER: A PROGRAMMED TECHNIQUE DESCRIBED THROUGH SYNTHETIC SEISMOGRAMS IN NEAR-SURFACE

*** Özcan ÇAKIR**

[1] *Süleyman Demirel University, Engineering and Natural Sciences Faculty, Geophysics Department, Isparta, TÜRKİYE*
ozcancakir@sdu.edu.tr

(Received: 22.09.2024; Accepted in Revised Form: 16.01.2025)

ABSTRACT: The knowledge of near-surface shear-vibration speed (i.e., V_{S30}) is crucial to properly define the dynamic characteristic of shallow subsurface in the earthquake mitigation efforts. In this respect, we propose a programmed technique in which the Rayleigh surface vibrations are solved for the determination of two-dimensional (2D) speed structure (vertically polarized shear-vibration – V_{SV}) in terms of fundamental mode (FM) dispersal curves (both group and phase speeds). The synthetic seismograms are calculated to simulate the real Earth and then the three data processing procedures, i.e., the weighted preconditioned linear radon transform (WPLRT), one-station (OS) approach and double-station (DS) approach, are sequentially applied to these synthetics. The common-shot gather (CSG) is assumed as data collection geometry. The WPLRT is first used to produce a phase speed dispersal curve from which the one-dimensional (1D) V_{SV} structure corresponding to the average structure underneath the CSG is inverted. The average 1D V_{SV} structure between the source and receiver is next inverted using the OS group speed dispersal curve where the number of OS curves is proportional to the number of geophones. In the third step, the average 1D V_{SV} structure corresponding to the DS pathway is inverted utilizing the group and phase speed curves where the number of DS curves is proportional to the number of inter-station pathways. Hundreds of dispersal curves (both group and phase speeds) take place in each step of the proposed technique. To select the associated dispersal curve, a programmed scheme is established. The studied area is described in terms of grid points and then the OS and DS dispersal curves are transferred into unique dispersal curves at these grid points for which a set of linear systems defined through travel times are solved. A pseudo 2D cross-section beneath the studied area is eventually established by merging the 1D V_{SV} structures found by the inversion of dispersal curves at grid points.

Keywords: *Inversion, Radon Transform, Rayleigh Surface Waves, One-Station, Double-*Station

1. INTRODUCTION

Geophysical, geological, and geotechnical engineers are eager to learn about the physical conditions of the subsurface material in the Earth for which geophysical engineering offers non-invasive techniques [1, 2, 3]. There exist several diverse reasons triggering this interest in the subsurface structure. Seismic hazards (e.g., liquefaction and landslides) [4], exploration for underground resources (e.g., rare earth elements) [5], need for long-term endurance of the geotechnical structures (e.g., subways, excavations and dams) [6] and environmental concerns (e.g., underground pollution) [7] are some of these main reasons. The geophysical engineering employs different methods (i.e., seismic, electrical, gravity and magnetics) [8] to image the subsurface structure where different physical parameters (e.g., seismic speed, density, electrical resistivity, and magnetic susceptibility) are measured. The seismic method employing the elastic vibrations (i.e., compressional, shear and surface waves) [9] provide effective tools to characterize the distribution of subsurface seismic speeds in multi-dimensions. Several seismic sources (i.e., earthquakes, explosions, impact sources, vibrators, and ambient noise) initiate elastic vibrations in the subsurface and then a set of receivers (i.e., geophones, hydrophones, seismometers, and

***Corresponding Author:** Özcan ÇAKIR, ozcancakir@sdu.edu.tr

accelerometers) located at certain distance from the source is used to record the incoming vibrations. One-dimensional (linear) or two-dimensional (circular, triangular, orthogonal grid or custom) receiver array distributions are commonly employed in the field. Elastic vibrations generated by multiple sources are recorded by each receiver in the array creating tomographic ray paths between sources and receivers. The compressional (P) and shear (S) speeds and group and phase speeds of surface waves (Rayleigh and Love) are measured along each ray path from which tomographic speed images are generated corresponding to the subsurface beneath the region of interest [10].

In real world applications, it is desirable to jointly consider data from diverse backgrounds (i.e., geophysical, geological, and geotechnical) for better interpretation of the studied area. For instance, lithological data from geological observations and standard penetration tests performed during geotechnical engineering practices should be considered together with the geophysical data to prevent misinterpretations. It is desirable to consider these different geophysical methods (i.e., seismic, electrical, gravity and magnetics) together so that the observed data volume can be significantly increased in a way that the subsurface is measured using different physical parameters (i.e., seismic, electrical, gravity and magnetics). The latter should make the modelling efforts more sensitive to the underground structure. However, the geophysical field survey is typically restricted by several factors, e.g., survey budget, geophysics equipment available for data collection and field conditions. In case of the seismic method, the field survey may include both body waves (compressional and shear) and surface waves (Rayleigh and Love) or may be limited to just body waves or surface waves. Herein we study the fundamental mode Rayleigh surface waves propagating in the shallow underground. The MASW (Multi-channel Analysis of Surface Waves) is a well-known acronym for shallow surface waves analysis [11, 12, 13]. The surface wave methods mostly employ active sources (i.e., sledgehammer, explosion, impact source and vibrator) as well as earthquakes, but recent applications utilize ambient noise (passive source) to extract surface waves embedded in noise recordings [14, 15, 16]. The REMI (Refraction Microtremor) [17, 18] and SPAC (Spatial Autocorrelation) originally proposed by Aki (1957) [19] are two methods applied to noise recordings.

The seismic surface waves acquired through either active source or passive source are frequently utilized to predict the shear-wave speeds in the subsurface [20, 21, 22, 23]. The passive data processing with the SPAC method calculates dispersion curves by comparing observed SPAC traces (cross-correlation functions between two stations) and theoretical Bessel functions [24] while the active data processing with the MASW method employs an integral transformation to the frequency-domain waveforms to compute the phase velocities between stations in the linear station array [11, 25]. The one-dimensional (1D) MASW surveying involves a common-shot gather (CSG) where a set of receivers aligned along a (pseudo) linear line records the surface waves emanating away from the source. The shear-wave velocity-depth profile representing the average structure beneath the receiver array is solved through the 1D MASW. In the two-dimensional (2D) MASW, the CSG geometry is laterally shifted to the right or left so that the 2D variations of the subsurface is measured along extended straight lines. In the present work, we employ one-station (group speeds), double-station (group and phase speeds) and array (phase speeds) analysis of geophone recordings in a CSG. These three analysis methods are commonly employed in global seismology [26, 27] and are currently adapted for shallow seismic applications. To the best of our knowledge, the proposed algorithm jointly considering multiple sets of active Rayleigh surface wave data in terms of both group and phase speeds is the first time reported for the respective literature.

We evaluate the performance of the proposed data processing technique by selecting a model structure to represent the near-surface ($\leq$ 40-m depth) speed variation in which the synthetic seismograms of Rayleigh surface waves in the vertical component are computed to simulate the wave propagation. The one-station approach results in a group speed dispersal curve representing the average structure between the source and receiver. The double-station approach works on the cross-correlogram computed from two stations in the geophone spread, which yields both group and phase speed dispersal curves representative of the average structure between the two receivers. The array analysis of

the geophone spread is performed based on the weighted preconditioned linear radon transform, which results a phase speed dispersal curve standing for the average structure underneath the geophone spread. All these dispersal curves are combined to invert the 2D shear-wave velocity structure underneath the CSG.

2. MATERIAL AND METHODS

2.1. Model Structure

It is essential that geophysical numerical methods suggested for the data processing are assessed for performance before they are applied to real-world data collections. In the case of seismic methods, synthetic seismograms are ideal candidates to perform the necessary test processes. We aim to solve the V_{SV} (vertically polarized shear-vibration) structure in the near surface ($\leq$ 40-m depth) for which we consider a representative model structure as listed in Table 1. The model structure is one-dimensional with multiple depth sections where each depth section is represented by compressional (V_P) and vertically polarized shear (V_{SV}) speeds, density (d) and compressional (Q_P) and shear (Q_S) quality factors. In Table 1, based on the seismic speeds, each depth section is characterized according to its stiffness as soft, softer, hard, and harder above the half space corresponding to the basement rocks.

Table 1: Model structure with a low-speed zone (LSZ) in the middle depth section. The depth sections are considered Poisson solid, i.e., $V_P = \sqrt{3}V_{SV}$. The density is computed from $d = 0.32V_P + 0.77$ [28]. The shear-vibration quality factor is set to $Q_S = Q_P/2$.

Depth sections (m)	V_P (m/s)	V_{SV} (m/s)	d (gr/cm^3)	Q_P	Stiffness
2	693	400	1.00	200	Softer near
2	1039	600	1.10	200	surface
2	1386	800	1.21	300	
2	1559	900	1.27	400	Hard middle
6	1732	1000	1.32	400	layers
6	1386	800	1.21	300	LSZ
6	1472	850	1.24	300	
2	1732	1000	1.32	500	Hard lower
2	1905	1100	1.38	500	layers
10	1992-2061	1150-1190	1.41-1.43	500	Harder transition
∞	2078	1200	1.44	500	Basement rocks

Figure 1 shows the data collection geometry (i.e., common-shot gather – CSG) as well as the data processing schemes consistent with the one-station, double-station, and array analysis. Each geophone (solid triangle) in the array records the seismic energy arrivals created by the source at the shot point to the right. A vertical source (e.g., accelerated weight drop) and vertical geophones are considered. The geophone recordings are processed to extract the Rayleigh surface vibration dispersal curves (phase and group speed). The recordings are processed either alone for the one-station group speeds (*i*), together for the double-station phase and group speeds (*ii*) or all together for the array analysis of phase speeds (*iii*). The grid points (solid circles) refer to the intervals between geophones. The first grid point (indexed zero in Figure 1) corresponds to the distance range in the near offset. A linear system processing the Rayleigh surface vibration in terms of the group and phase arrival times is utilized to determine the 1D speed-depth profile corresponding to each grid point. The 1D solutions are then combined to attain the 2D speed structure underneath the CSG.

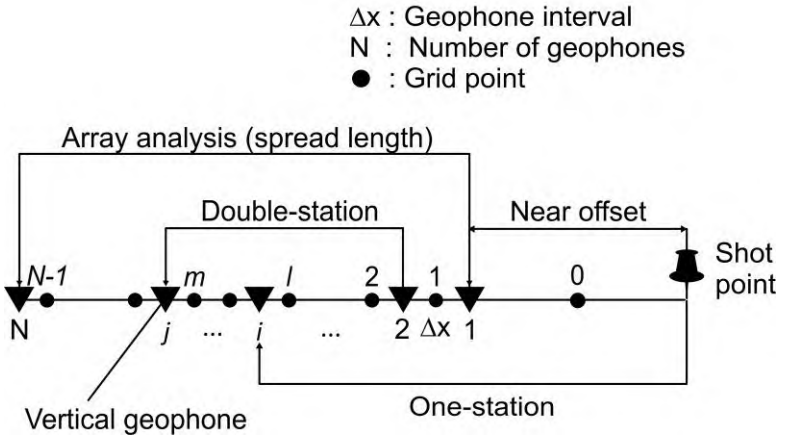

Figure 1: Spread configuration for the common-shot gather – CSG. The shot point is a P-vibration generator, and the vertical geophones record vertical (V) component displacement. Both shot point and geophones are placed at the surface. One-station geometry between source and geophone, double-station geometry between geophone pairs, and array geometry including all geophones are indicated.

2.2. Synthetic Seismograms

There are certain parameters that we need to set up for the CSG before the synthetic seismograms are computed. The near offset measuring the distance between the shot point and the first geophone in the geophone array is set to 30 m. With increasing offset the surface vibration energy reaches greater depth of penetration, and the fundamental mode (FM) separates better from the overtones. However, if the offset gets longer, then sending the surface vibration energy to greater distances becomes increasingly difficult because of anelastic attenuation. Therefore, the near offset (see Figure 1) should be chosen to meet the requirements of the respective field surveying. The geophone interval (Δx) in the array is set to 2 m. The horizontal resolution of the CSG is proportional to Δx, i.e., better horizontal resolution is obtained with smaller Δx. The number of geophones is set to N=60, which determines the spread length. The distance to the last geophone (i.e., N) in the array establishes the maximum possible depth of penetration. An even deeper depth of penetration is possible if N is further increased to, for instance, N=120, but then a stronger seismic source (double strength) should be preferred to deliver the seismic energy to such greater distances. The sample interval of the computed seismograms is $\Delta t = 0.25$ ms while the record length is set to 1 s, which is a time length good enough to include all the seismic energy arrivals at current geophone locations. A vertical impact source with a parabolic pulse shape of base $4\Delta t$ is assumed to produce the seismic vibrations.

For the current numerical calculations, we mostly employ the software package by Herrmann (2002) [29]. Figure 2 displays the synthetic shot-record corresponding to the model structure in Table 1. The display gains are adjusted according to the maximum amplitudes at each receiver location so that the designated space for each trace is optimized in the shot window. The Rayleigh surface vibrations show complex pattern of amplitude highs and lows with travel time indicating both normal and reverse dispersals due to vertically heterogeneous subsurface and interference from higher modes. In addition, the waveforms spread in time with increasing geophone distance (see orange color lines).

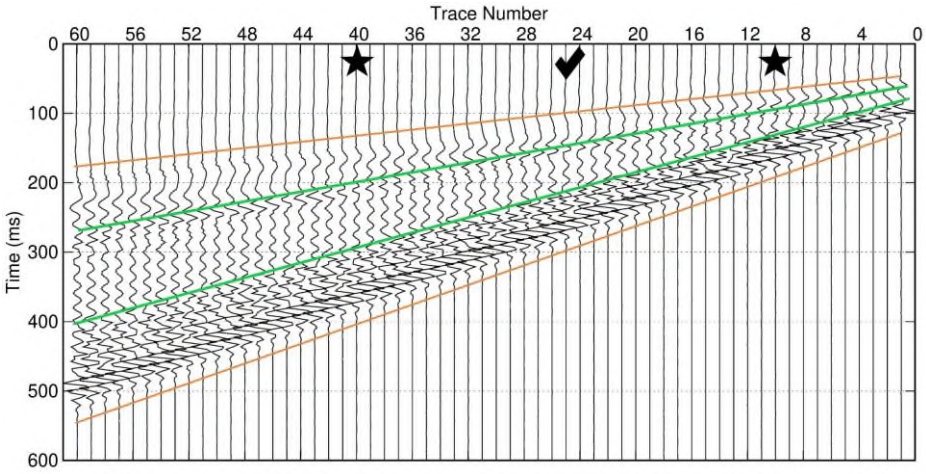

Figure 2: Vertical component Rayleigh synthetic seismograms are shown. Source is a vertical impact (see Figure 1). Stars indicate geophone locations (#10 and #40) used to demonstrate sample calculations of double-station (DS) approach. Tick mark stands for geophone location (#25) used for sample calculations of one-station (OS) approach.

2.3. Array Analysis of Seismograms

We employ the weighted preconditioned linear radon transform (WPLRT) to compute the phase speeds corresponding to the subsurface beneath the geophone spread. The LRT considers the plane-wave decomposition of the wavefield through the following relation [30].

$$\boldsymbol{d} = \boldsymbol{L}\boldsymbol{m} \tag{1}$$

where $\boldsymbol{d}$ and $\boldsymbol{m}$ represent the CSG and radon panel, respectively, which are connected by the forward operator $\boldsymbol{L}$ defined by complex exponential $\boldsymbol{L} = e^{jkx}$. The operator $\boldsymbol{L}$ employs the travel distance x and wavenumber $k = \omega/c$ where ω is the angular frequency (rad/s) and c is the phase speed (m/s). The following linear system is used to solve the radon panel $\boldsymbol{m}$.

$$\left(\boldsymbol{W}_{\boldsymbol{m}}^{-\boldsymbol{T}}\boldsymbol{L}^{\boldsymbol{T}}\boldsymbol{W}_{\boldsymbol{d}}^{\boldsymbol{T}}\boldsymbol{W}_{\boldsymbol{d}}\boldsymbol{L}\boldsymbol{W}_{\boldsymbol{m}}^{-\boldsymbol{1}} + \lambda\boldsymbol{I}\right)\boldsymbol{W}_{\boldsymbol{m}}\boldsymbol{m} = \boldsymbol{W}_{\boldsymbol{m}}^{-\boldsymbol{T}}\boldsymbol{L}^{\boldsymbol{T}}\boldsymbol{W}_{\boldsymbol{d}}^{\boldsymbol{T}}\boldsymbol{W}_{\boldsymbol{d}}\boldsymbol{d} \tag{2}$$

Herein $\boldsymbol{W}_{\boldsymbol{m}}$ is the matrix defining model weights, $\boldsymbol{W}_{\boldsymbol{d}}$ is the matrix for data weights, $\boldsymbol{I}$ is the identity matrix, λ is the operator condition number and $-\boldsymbol{T}$ stands for the transpose of inverse matrix. We solve Equation (2) by utilizing the conjugate gradient algorithm [15]. The radon panel $\boldsymbol{m}$ is a complex valued function of frequency (f) and phase speed (c). We build an (f, c) diagram using the spectral amplitudes $|\boldsymbol{m}|$ from which we pick the phase speed dispersal curves corresponding to the maximum amplitudes on the diagram.

2.4. One-Station Approach

The Rayleigh surface vibration data is collected through the CSG where the number of receivers is set to N=60. We apply the Multiple Filter Technique (MFT) to the Fourier transformed seismogram $S(\omega)$ at each receiver (geophone) location from which the (observed) fundamental mode (n=0) group speed curve is constructed. In the frequency (f) domain, the MFT utilizes the Gaussian filter $(\exp[-\alpha(f - f_c)^2/f_c^2])$ where f_c (Hz) is the filter center frequency at which point the one-station (OS) group speed is sought [29, 31]. The parameter α determines the resolution in the time and frequency domains. A higher (lower) α value corresponds to the higher (lower) resolution in the frequency domain

while the resolution inversely gets lower (higher) in the time domain. Therefore, there is a tradeoff between time and frequency domain resolutions. Different α values should be experimented to achieve better resolution of the observed dispersal curve throughout the MFT.

2.4.1. Linear system for one-station approach

The lateral extent covered by the CSG is discretized via some grid points (see Figure 1). At each grid point, the slowness is defined by $S = \Delta s + S_{ave}$ where Δs is the unknown slowness perturbation to the average slowness (i.e., S_{ave}), which is valid for both group (OS and/or DS) and phase (DS) arrival times. In this respect, we set up a linear system to solve the OS group arrival times as follows.

$$^{OS}\mathbf{C}\ {}^{\gamma}\mathbf{q} = {}^{OS}\mathbf{d} \tag{3}$$

where $\gamma = G$ representing the group speed and the system matrix $^{OS}\mathbf{C}_{N_1 xN}$ ($N_1 = {}^{OS}N_a$) is defined by the following matrix.

$$^{OS}\mathbf{C} = \begin{bmatrix} x_0 & 0 & \dots & 0 \\ x_0 & \Delta x & \dots & 0 \\ \vdots & \vdots & \ddots & \vdots \\ x_0 & \Delta x & \cdots & \Delta x \end{bmatrix} \tag{4}$$

Herein $^{OS}N_a = N$. The column vector $^{\gamma}\mathbf{q}_{Nx1}$ (unknown group slowness vector) in Equation (4) is given as follows.

$$^{G}\mathbf{q} = \begin{bmatrix} {}^{G}\Delta S^{(0)} \\ {}^{G}\Delta S^{(1)} \\ \vdots \\ {}^{G}\Delta S^{(N-1)} \end{bmatrix} \tag{5}$$

The elements of the column vector $^{OS}\mathbf{d}_{N_1 x1}$ (known group travel time vector) in Equation (4) have the following combined form.

$$^{OS}d_i = [x_0 + (i-1)\Delta x]\ {}^{OS}S_{obs}^{(i)} - x_0\ {}^{OS}S_{ave}^{(0)} - \Delta x \sum_{j=1}^{i-1} {}^{OS}S_{ave}^{(j)} \quad i = 1,2,\dots,N \tag{6}$$

where the $^{OS}S_{ave}^{(i)}$ is calculated from the observed slowness ($^{OS}S_{obs}^{(i)}$) by the application of the succeeding expression.

$$^{OS}S_{ave}^{(k)} = \frac{1}{N-k}\sum_{j=k+1}^{N} {}^{OS}S_{obs}^{(j)} \quad k = 0,1,\dots,N-1 \tag{7}$$

The following equation is used to compute the group travel times of OS Rayleigh surface vibrations.

$$^{OS}t^{(i)} = x_0\left(\Delta s^{(0)} + {}^{OS}S_{ave}^{(0)}\right) + \sum_{k=1}^{i-1}\Delta x\left(\Delta s^{(k)} + {}^{OS}S_{ave}^{(k)}\right) \quad i = 1,2,\dots,N \tag{8}$$

2.5. Double-Station Approach

The cross-correlation process measures the similarity between two signals. We utilize this property to quantify the phase speed $c(\omega)$ and group speed $u(\omega)$ between two stations [$A_1(\omega) = |A_1(\omega)|e^{-j\varphi_1(\omega)}$ and $A_2(\omega) = |A_2(\omega)|e^{-j\varphi_2(\omega)}$] in the receiver array. In the frequency domain, the cross-correlogram $A(\omega)$ is defined as follows.

$$A(\omega) = |A(\omega)|e^{-j\varphi(\omega)} \tag{9}$$

where $|A(\omega)| = |A_1(\omega)||A_2(\omega)|$ is the amplitude spectrum, $\varphi(\omega) = \varphi_2(\omega) - \varphi_1(\omega)$ is the phase

spectrum, $j = \sqrt{-1}$ and $\omega = 2\pi f$. The MFT is applied to the cross-correlogram $A(\omega)$ to resolve the double-station (DS) group speed $u(\omega)$. The phase spectrum $\varphi(\omega)$ is utilized to compute the DS phase speed $c(\omega)$ as follows.

$$c(\omega) = \omega x/[\varphi(\omega) + 2n\pi] \quad n = \cdots, -2, -1, 0, 1, 2, \cdots \tag{10}$$

Herein x describes the distance between two stations. There exists some ambiguity (or cycle skipping) in the phase speed measurement, which is quantified by the term $2n\pi$ in Equation 10. This issue of ambiguity is fixed by applying a method described in Çakır and Kutlu (2023) [32].

2.5.1. Linear system for double-station approach

We set up two linear systems to solve the DS data, i.e., one linear system for the phase arrival times and another one for the group arrival times. The respective system can be outlined as follows.

$$^{DS}\mathbf{C}\ {}^{\gamma}\mathbf{q} = {}^{DS}\mathbf{d} \tag{11}$$

where $\gamma = P$ (i.e., phase speed) or $\gamma = G$ (i.e., group speed). The system matrix $^{DS}\mathbf{C}_{N_2 \mathrm{x} N}$ ($N_2 = {}^{DS}N_a$) is defined by the following expression.

$$^{DS}c_{ij} = \begin{bmatrix} {}^{DS}y_{ij}^{(0)} \\ {}^{DS}y_{ij}^{(1)} \\ \vdots \\ {}^{DS}y_{ij}^{(N_d-1)} \end{bmatrix} \quad i = 1,2,\ldots,N_d(N_d+1)/2\,,\ \ j = 1,2,\ldots,N-1 \tag{12}$$

where

$$^{DS}y_{ij}^{(m)} = \begin{Bmatrix} \Delta x & i = 1,\ldots,N_d - m\,,\ \ j = m+1,\ldots,m+N_c+i-1 \\ 0 & \text{otherwise} \end{Bmatrix}\ m = 0,1,\ldots,N_d-1 \tag{13}$$

$$^{DS}N_a = N_d(N_d+1)/2 \tag{14}$$

$$N_d = N - N_c \tag{15}$$

Herein $N_c = 30$ defines the minimum number of geophone intervals between two stations. The column vector $^{\gamma}\mathbf{q}_{N_2 \mathrm{x} 1}$ (unknown phase or group slowness vector) in Equation (11) is given as follows.

$$^{P,G}\mathbf{q} = \begin{bmatrix} {}^{P,G}\Delta S^{(1)} \\ {}^{P,G}\Delta S^{(2)} \\ \vdots \\ {}^{P,G}\Delta S^{(N-1)} \end{bmatrix} \tag{16}$$

The column vector $^{DS}\mathbf{d}_{N_2 \mathrm{x} 1}$ (known phase or group travel time vector) in Equation (11) has the following composite form.

$$^{DS}d_i = (j-1)\Delta x\ {}^{DS}S_{obs}^{(i,j)} - \Delta x \sum_{j=1}^{i-1} {}^{DS}S_{ave}^{(j)} \quad i = 1,2,\ldots,N_d\,,\ \ j = N_c + i,\ldots,N \tag{17}$$

The observed phase or group slowness denoted by the $^{DS}S_{obs}^{(i)}$ is utilized to calculate the average phase or group slowness $^{DS}S_{ave}^{(i)}$ via the subsequent expressions.

$$^{DS}S_{ave}^{(k)} = \frac{1}{k[N_d-(k-1)/2]}\sum_{i=1}^{k}\sum_{j=N_c+i}^{N} {}^{DS}S_{obs}^{(i,j)} \quad k = 1,2,\dots,N_d \tag{18}$$

$$^{DS}S_{ave}^{(k)} = {}^{DS}S_{ave}^{(N-N_c)} \quad k = N_d+1,\dots,N \tag{19}$$

The phase or group travel times of DS Rayleigh surface vibrations are determined by the application of the below expression.

$$^{DS}t_i^{(j)} = \sum_{k=i}^{j}\Delta x(\,\Delta s^{(k)} + {}^{DS}S_{ave}^{(k)}) \quad i = 1,2,\dots,N_d\,,\;\; j = N_c+i,\dots,N \tag{20}$$

3. NUMERICAL RESULTS

3.1. Application of Array Analysis

The WPLRT is applied to the model structure and Figure 3a shows the result. The theoretical phase speed curves for the fundamental plus higher modes are demonstrated by the blue lines. The spectral amplitudes $|\boldsymbol{m}|$ characterized by the red color distinctly exhibit the fundamental mode (n=0), which is prevalent on the recordings. The higher modes (n=3, 4 …) are represented by weak amplitudes on the seismograms and are absent on the (f, c) diagram. On the other hand, the higher modes (n=1, 2) are represented by some spectral amplitudes $|\boldsymbol{m}|$ as shown by the black color arrow. The mode mingling [33, 34] prevents us from separating these modes from each other and therefore we did not consider this part of the phase speed spectrum in the structural inversion. The black dots showing the locations of the maximum $|\boldsymbol{m}|$ values at each frequency (Hz) correspond to the fundamental mode (FM). As indicated by the purple color arrows, at low frequencies (< 20 Hz) these black dots show some scattering around the true values (i.e., blue line). The actual surface vibrations are guided by cylindrical wavefronts and therefore our plane-wave decomposition is not exact. The latter case called near field effect [35] is particularly eminent on the low frequency surface vibrations. To increase the near offset (see Figure 1) should be helpful to alleviate this disturbance on the (observed) phase speed curve.

In Figure 3b, we show the inversion result of the (observed) phase speed curve (black color symbols – FM attained from the WPLRT approach in Figure 3a), which aims to resolve the average 1D speed-depth distribution underneath the geophone array. A linearized inversion method [36, 37, 38, 39] initially starting with a half-space model (blue line in Figure 3b) is employed. Figure 3c displays the resulting phase speed fit after the inversion. In Figures 3b and 3c, the inverted (theoretical) 1D model and phase speed curves are shown by the red (green) color. The purple color arrows in Figure 3c indicate that the longer period phase speeds (c) are poorly resolved in the inversion. Moreover, the underground speed jumps as indicated by the cyan color arrows in Figure 3b are determined as more like speed gradients.

3.2 Group Speeds

In surface wave dispersion analysis, meddling (or interference) between the fundamental mode and higher modes (i.e., different modes crossing and touching each other) may occur. Therefore, one needs to be careful against the mode mixing events, e.g., apply some filtering and time windowing before the dispersal analysis. In Figure 4, we show the fundamental (n=0) and higher mode (n=1, 2, 3…) group speed (u) dispersal curves calculated for the theoretical model in Table 1. The group speed curves exhibit some mixing between higher modes (n=1, 2 – indicated by orange color arrow) for frequencies around 45 Hz and then the mode mixing event becomes worse at higher frequencies (> 55 Hz) among other higher modes (n=2, 3, 4 as pointed out by blue color arrow). On the other hand, the fundamental mode (n=0) made of both normal and reverse dispersal is free of any interference from the higher modes for the full frequency range 6-100 Hz.

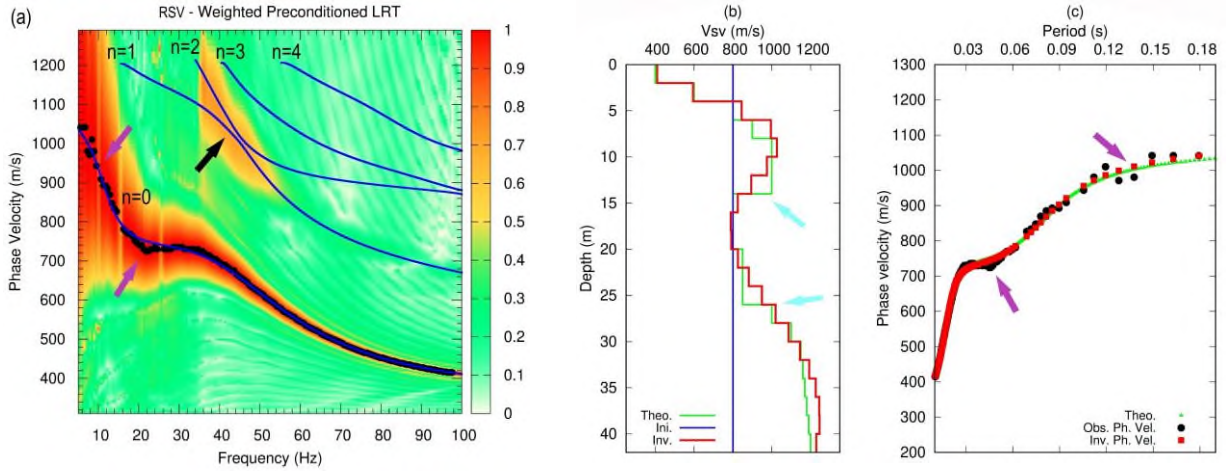

Figure 3: (a) The result of weighted preconditioned linear radon transform (WPLRT) is shown where the blue lines show the theoretical phase speed curves for the fundamental (n=0) plus higher modes (n=1, 2, 3 …). The fundamental mode (FM) selected from the WPLRT amplitudes represented by the black dots is inverted. (b) The inverted 1D speed structure represented by the red color line is shown where the initial model (blue line) and the theoretical model (green line) are also shown. (c) The inverted (red color), observed (black color) and theoretical (green color) dispersal curves are illustrated.

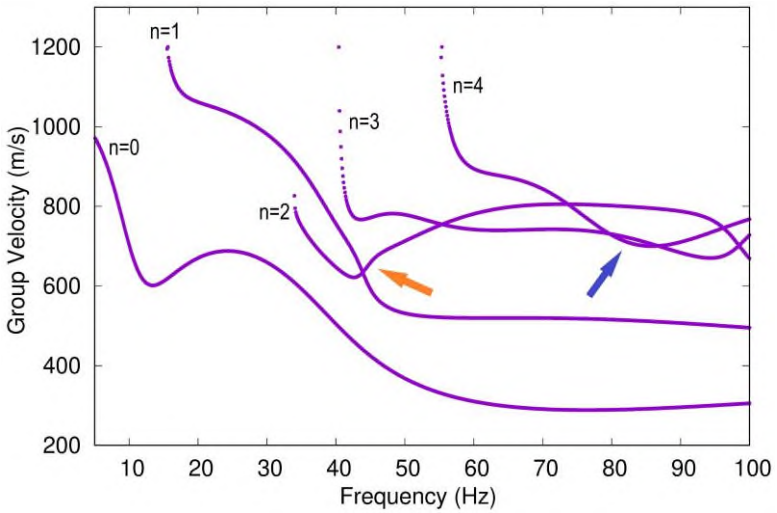

Figure 4: Theoretical group speed dispersal curves computed for the model structure in Table 1 are shown. Fundamental mode (n=0) and higher modes (n=1, 2, 3 …) are indicated. The orange and blue color arrows point to the higher mode group velocity curves crossing each other.

3.3. Application of One-Station Approach

The model structure (Table 1) includes velocity highs and lows changing with depth, which results Rayleigh surface waveforms showing complex pattern of amplitude highs and lows varying with time (see green lines in Figure 2). To manage such a complex amplitude pattern in the MFT analysis, we employ α values changing with period. For longer periods (> 0.1 s), we employ a smaller α value set to $\alpha = 12$, which means that we have lower resolution in the frequency domain but higher resolution in the time domain. The α value is increased to $\alpha = 40$ for shorter periods (≤ 0.1 s) so that a higher resolution in the frequency domain is attained. The latter means that we sacrifice some time domain resolution. Figure 5 shows the MFT results realized for geophone location #25, which is offset by 78 m (see Figure 2). Figure 5a displays the MFT result obtained by $\alpha = 40$ and Figure 5b by $\alpha = 12$ where color coding is

used in the MFT amplitudes. The highest resolution of the group speeds is achieved on the (f, u) diagram represented by the red color and then a gradual loss in the resolution occurs as indicated by the MFT amplitudes from orange to green color. The Rayleigh surface wave seismogram is provided on the right in each panel. The OS group speed curve representing the geophone location #25 is constructed by combining the two parts indicated by these white color circles in Figures 5a and 5b. The black color arrow in Figure 5b exhibits that the group speed curve is disrupted when $\alpha = 12$, but this disruption is alleviated when $\alpha = 40$ (Figure 5a). The cyan color arrow in Figure 5a shows that the lower frequency (or longer period) group speeds are slightly incorrect when $\alpha = 40$, but gets better when $\alpha = 12$ (Figure 5b).

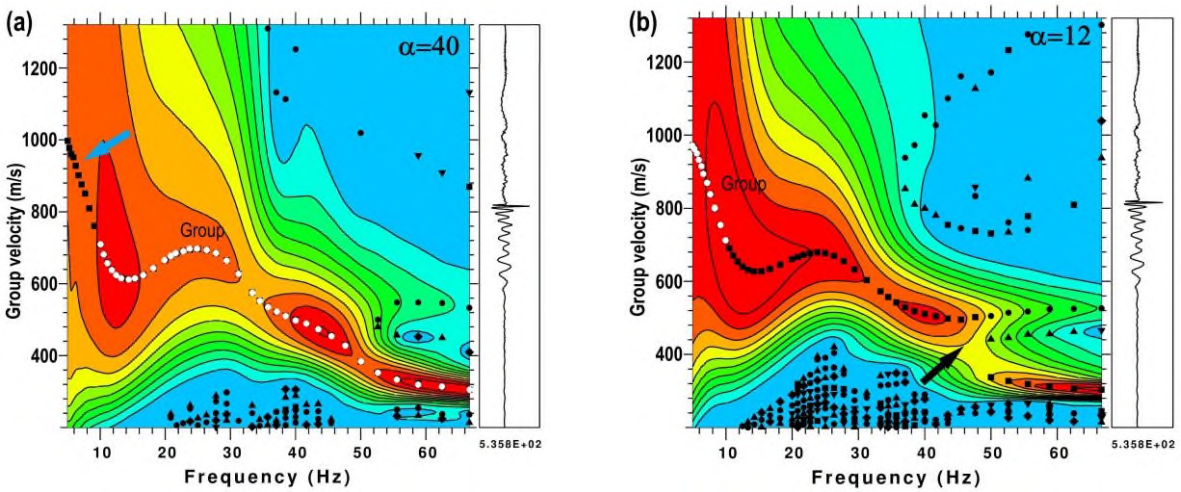

Figure 5: One-station (OS) approach applied to the model structure is shown at geophone location #25 indicated by a tick mark in Figure 2. Results of MFT at two different α values are shown. a) $\alpha = 40$ and b) $\alpha = 12$.

Figure 6a shows the (observed) group speed curve (blue color symbols) constructed by combining the two parts in Figures 5a and 5b (i.e., maximum MFT amplitudes denoted by white color symbols). This curve is inverted to reveal the average 1D speed-depth distribution beneath the distance range between the source and geophone location #25 (Figure 6b). A linearized inversion technique such as applied in Figure 3 is also utilized for this inversion, but this time the initial model (blue line in Figure 6b) is obtained from the inversion in Figure 3b (red line). Figure 6c shows the group speed fit reached after the inversion. The inverted (theoretical) 1D model is depicted by the red (green) color in Figure 6b.

The inverted (observed) group speed curve is displayed in the red (black) color in Figure 6c. Like Figure 3, the cyan color arrows in Figure 6b specify that the underground speed jumps are inverted as more like speed gradients. Moreover, the black color arrow in Figure 6a indicates that the shorter period (< 0.035 s) group speeds are acquired with some error (< 40 m/s), which causes the group speed mismatch between the observed and inverted, which is pointed out by the black color arrow in Figure 6c.

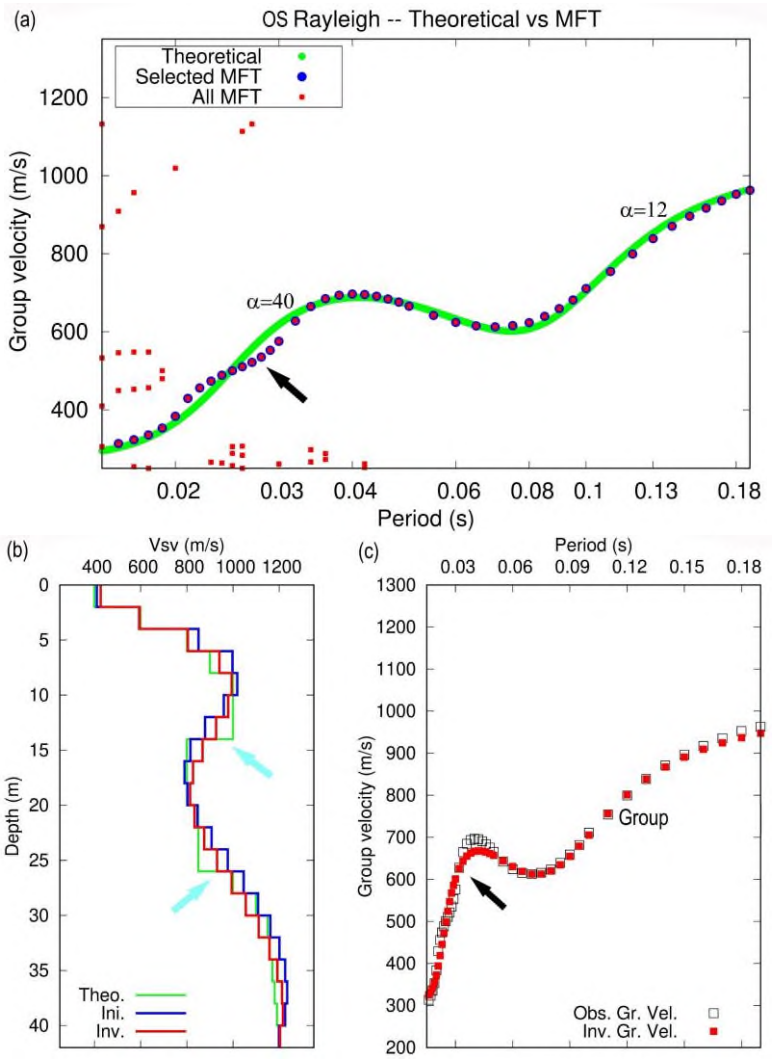

Figure 6: a) The fundamental mode (FM) group speed dispersal curve obtained from the combination of white dots in Figures 5a and 5b is shown where the theoretical group speed (green color), selected MFT group speed (blue color), and all computed MFT group speed (red color) are indicated. The FM group speed curve is inverted. (b) The inverted 1D speed structure (red color), initial model (blue color) and theoretical model (green color) are illustrated. (c) The observed (black color) and inverted (red color) group dispersal curves are shown.

3.3.1. Group speed result of one-station approach

We repeat the one-station (OS) approach presented in Figure 5 for every other geophone location in the receiver array, which yields FM group speed curves totaling to ${}^{OS}N_a = 60$. The corresponding MFT amplitudes illustrated by purple color solid circles are superimposed in Figure 7. We have computed the group speed curve using the inverted model in Figure 3, which is illustrated by the green color curve. The latter curve is utilized to produce the upper (cyan color) and lower (orange color) boundary curves. The interval width between these boundary curves increases from short to longer period, i.e., the width

is 160 m/s at 0.02-s period and increases to 310 m/s at 0.18-s period. This interval is employed as a selection range to bracket the OS group speed curves at all geophone locations. These MFT amplitudes corresponding to the FM staying outside the respective interval as pointed out by the yellow color arrow in Figure 7 are discarded during the process of dispersal curve selection.

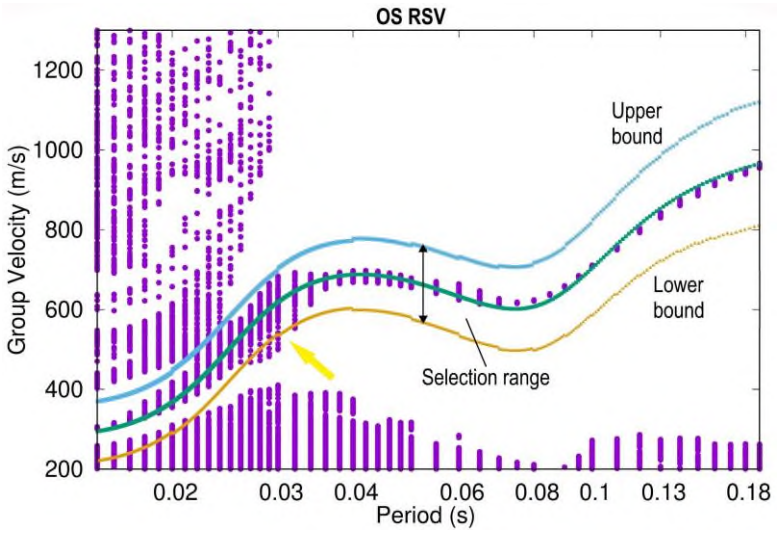

Figure 7: Purple color symbols correspond to the one-station (OS) MFT results. All the results at multiple geophone locations are shown superimposed. Rayleigh surface vibration (RSV) group speeds are chosen when staying between the upper (cyan color) and lower (orange color) boundaries.

3.4. Application of Double-Station Approach

We employ two seismogram records at geophone locations #10 (offset by 48 m) and #40 (offset by 108 m) for the DS approach. The corresponding cross-correlogram is calculated by the correlation of respective seismograms. Figure 8 illustrates the resulting group and phase speed diagrams. The MFT results, which are color coded changing from highest (red color) to lowest resolution (green color), are shown in two parts, i.e., the first part (Figure 8a) is attained by setting the α value to $\alpha = 40$ and the second part (Figure 8b) to $\alpha = 12$. In Figures 8a and 8b, the cross-correlogram is demonstrated on the right. The DS group speed curve $u(\omega)$ representing the inter-station distance between the two geophones (#10 and #40) is built by merging the two parts specified by these white color circles in Figures 8a and 8b. The group speed (FM) resolution tends to be interrupted when $\alpha = 12$ as pointed out by the black color arrow in Figure 8b. The latter resolution improves when $\alpha = 40$ (Figure 8a). The longer period (or lower frequency) group speeds are inaccurate when $\alpha = 40$ as pointed out by the brown color arrow in Figure 8a. The corresponding group speeds improve when $\alpha = 12$ (Figure 5b). The result of DS phase speed $c(\omega)$ analysis is provided in Figure 8c. The black color symbols represent these branches resulting from different n values in $2n\pi$ where the FM phase speed curve $c(\omega)$ is depicted by the red color symbols.

In Figure 9a, we illustrate the (observed) group speed curve (blue color symbols) versus period assembled by joining the two parts in Figures 8a and 8b (i.e., white color symbols). As pointed out by the orange color arrows (Figure 9a), some shorter period group speeds are excluded since they stay outside the selection range (see Figure 10). On the other hand, Figure 9b displays the (observed) phase speed curve (blue color symbols) versus period converted from Figure 8c. By utilizing the linearized inversion technique like applied in Figure 6, we invert the latter group and phase speed curves to determine the 1D V_{SV} structure (Figure 9c). This joint inversion of $u(\omega)$ and $c(\omega)$ represents the average speed structure between the two geophones (#10 and #40) considered in the DS analysis and the subsequent dispersal

curve fits are shown in Figure 9d. The red (green) color depicts the inverted (theoretical) 1D model in Figure 9c while the red (black) color displays the inverted (observed) group and phase speed curves in Figure 9d. Like Figures 3 and 6, the underground speed jumps are inverted as more like speed gradients (see cyan color arrows in Figure 9c). Moreover, the black color arrow in Figure 9a indicates that the group speeds around 0.045 s period exhibit some error (< 30 m/s), which causes relative group speed mismatch between the inverted and observed (see black color arrow in Figure 9d).

3.4.1. Phase and group speed results of double-station approach

Multiple inter-station pathways exist in the DS approach. For the minimum path length, we enforce a restriction described by $\Delta l = N_c \Delta x = 60$ m where Δx is the geophone interval (set to 2 m) and N_c is the minimum number of geophone intervals between two stations (set to 30). The expression $[{}^{DS}N_a = N_d(N_d + 1)/2]$ defines the total number of DS pathways where $N_d = N - N_c$. We utilize $N = 60$ which produces ${}^{DS}N_a = 465$. The expression $[L = (N - 1)\Delta x]$ defines the maximum inter-station distance where the inter-station distances change in the range 60-118 m. The process explained in Figure 9 is repeated for all occurrences of the DS approach. All the DS group (Figure 10a), and phase (Figure 10b) speed results (purple color solid circles) are assembled to show them superimposed. The inverted model in Figure 3b (red color) is employed to calculate the group and phase speed curves shown by the green color curves in each panel. The selection range for the DS group and phase speeds is created by the upper (cyan color) and lower (orange color) boundary curves. This range has variable width changing with period, which is 160 m/s at a shorter period (i.e., 0.02 s) and then increases to 310 m/s at a longer period (i.e., 0.18 s). For all inter-station distances, these intervals, which are the same for both group and phase speeds, are employed as the selection ranges to bracket the DS dispersal data.

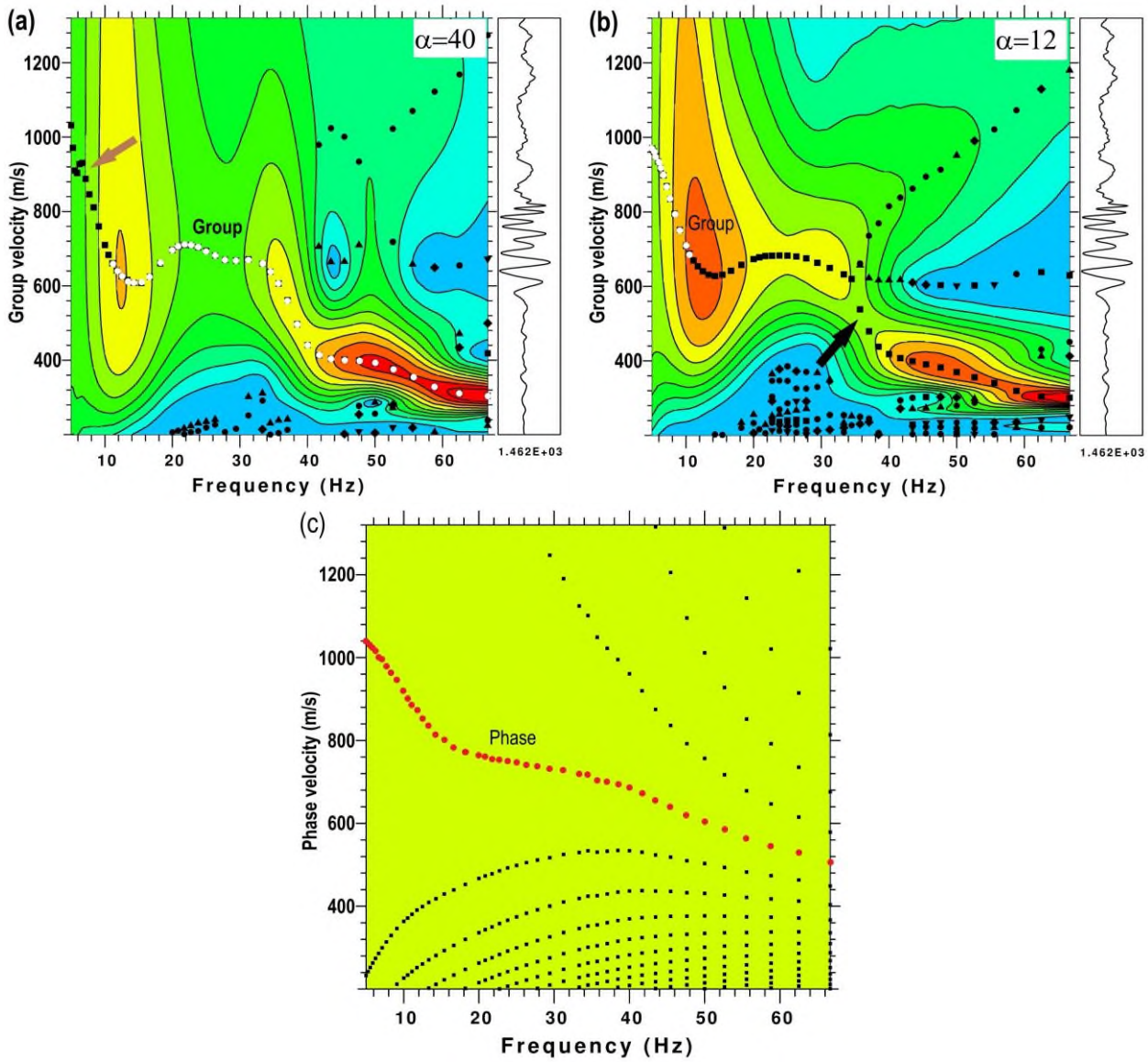

Figure 8: Rayleigh surface wave propagation between geophone locations #10 and #40 indicated by two stars in Figure 2 is shown using the double-station (DS) approach applied to the model structure. The DS MFT results employing two different α values are illustrated. a) $\alpha = 40$ and b) $\alpha = 12$. The phase speed cycles are displayed in (c). The fundamental model (FM) phase speed curve is indicated by the red color.

Both OS group speeds (see yellow arrow in Figure 7) and DS group and phase speeds (see yellow arrows in Figure 10) develop some uncertainties at specifically shorter periods (< 0.04 s), i.e., the inconsistency surrounding the green color dispersal curve. To attain more accurate group and phase speed results one may need to choose a smaller time sampling (e.g., $\Delta t = 0.1$ ms instead of current $\Delta t = 0.25$ ms). In addition, one may work on the α parameter for fine tuning, i.e., various α values other than $\alpha = 42$, which is currently preferred, could be evaluated to see if any improvement is gained. The MFT is a sizable procedure to complete, which has overall time complexity of $O(N^2 \log N)$ at numerous geophone positions (${}^{OS}N_a$) and inter-station spaces (${}^{DS}N_a$). We were not able to trail the calculations using finer parameters (i.e., Δt and α) since we have limited computational power in terms of memory – RAM and processor – CPU. Therefore, we stay with the existing parameters.

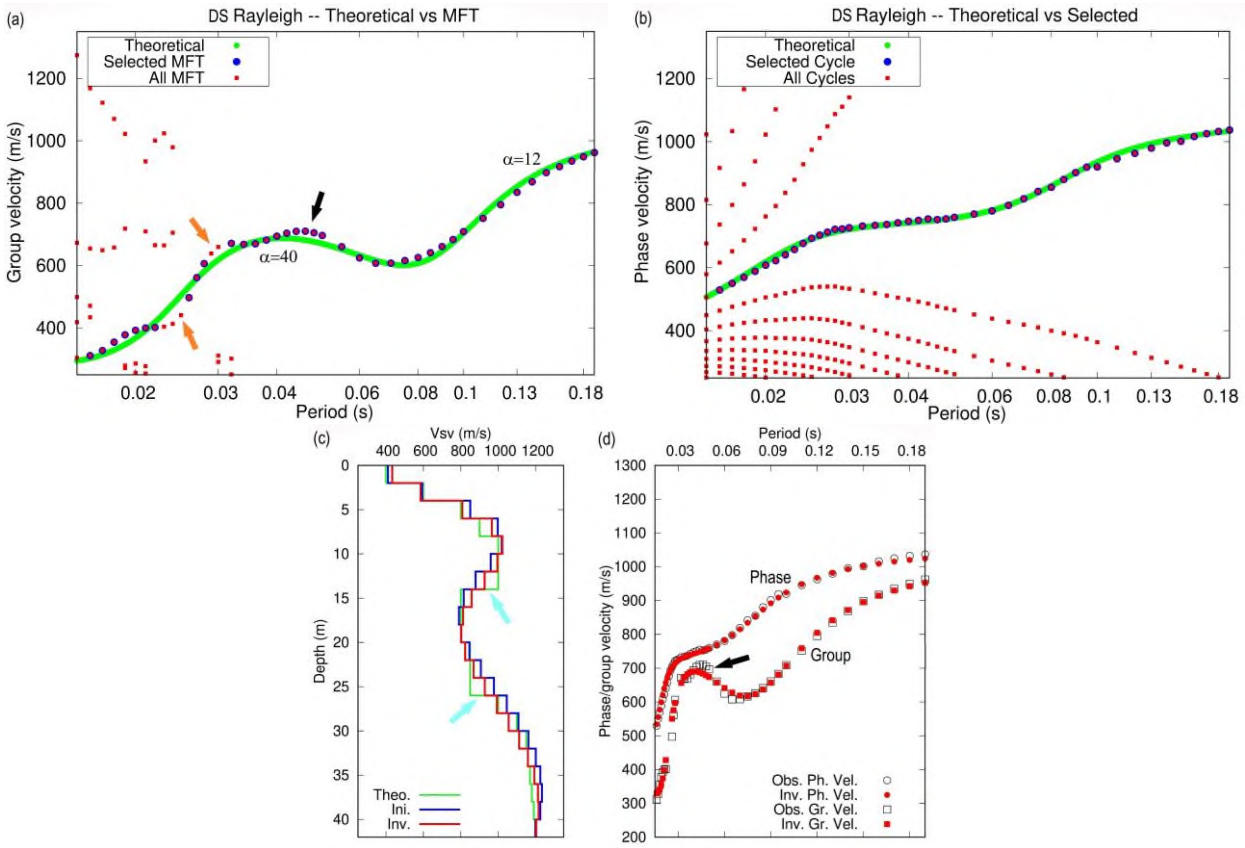

Figure 9: a) The white dots in Figures 8a and 8b are combined to get the fundamental mode (FM) group speed dispersal curve where the theoretical group speed (green color), selected MFT group speed (blue color), and all computed MFT group speed (red color) are specified. The phase speed cycles are displayed in (b) where the theoretical phase speed (green color), selected cycle (blue color), and all computed cycles (red color) are indicated. The FM group and phase speed curves are jointly inverted. (c) The inverted 1D speed structure (red color), initial model (blue color) and theoretical model (green color) are displayed. (c) The observed (black color) and inverted (red color) group and phase dispersal curves are illustrated.

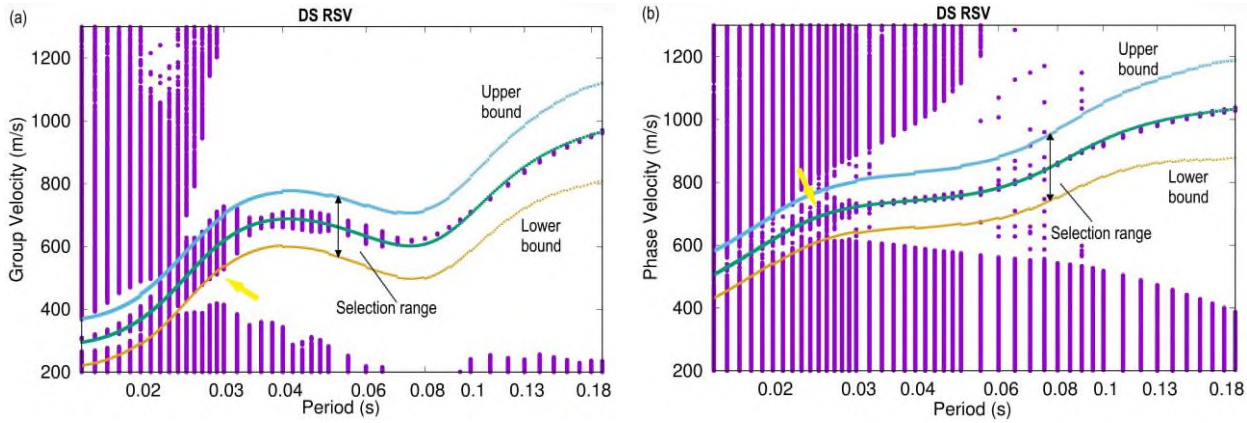

Figure 10: Double-station (DS) results (purple color symbols) are shown superimposed for multiple inter-station distances. (a) DS MFT results and (b) DS phase speed cycles. The upper (cyan color) and lower (orange color) boundaries specify the selection range of group and phase speeds of Rayleigh surface vibration (RSV) in (a) and (b).

One should note that we have considered seismograms without noise and yet the dispersal analysis still shows some disturbances (Figures 7 and 10). In actual measurements, the noise effect caused by three-dimensional (3D) scattering, multipathing and mode interferences [40, 41, 42, 43] might further create disturbances on the observed dispersal data. The selection ranges employed for the speed bracketing processes (Figures 7 and 10) should help resolve the disturbance issues persistent on the observed dispersal curves so that smoother inversions of the subsurface are achieved.

3.5. 2D Vertical Cross-Section Under Common-Shot Gather

There exist three linear systems to solve, i.e., one for the OS group arrival times and two for the DS group and phase arrival times. We chain all these three systems together to jointly solve the phase and group speed data to recover the 2D V_{SV} structure underneath the common-shot gather (CSG). First, the DS phase arrival times are solved through the respective linear system to find the phase slowness values at grid points (see Figure 1). Second, we merge the two linear systems consistent with the OS and DS group arrival times to resolve the group slowness values at the same grid points. The damped least squares method is employed for the solution of each linear system [29, 44, 45]. At each grid point, the phase and group speed dispersal curves are separately constructed by repetitively solving the above linear systems for each discrete frequency (Hz) value. To find the 1D V_{SV} structure beneath a grid point, the corresponding dispersal curves (phase and group speeds) are jointly inverted for which the inversion strategy used in Figure 9 is followed. The 2D V_{SV} cross-section corresponding to the structure underneath the CSG is finally built by combining all the 1D V_{SV} solutions together [46].

In Figure 11, we demonstrate the subsequent 2D cross-section where the speed changes with depth are shown. In the near surface from 0-m to 4-m depth, the speed structure is represented by two layers each with 2-m thickness where the V_{SV} speed increases from 400 m/s to 600 m/s. This two-layer structure is correctly resolved by the inverted speeds. The depth range from 4-m to 8-m includes two layers in which the V_{SV} speed rises from 800 m/s to 900 m/s, which is properly characterized by the inverted speeds but there exists slight resolution loss for this two-layer structure. Below this depth range the V_{SV} speed increments to 1000 m/s creating a high-speed zone (HSZ), which is suitably represented by the inverted speeds. There exists a speed reversal (i.e., low speed zone – LSZ) at 14-m depth in which the V_{SV} speed drops to 800 m/s, which is represented by the 2D cross-section (Figure 11). From 20-m to 30-m depth, the V_{SV} speed constantly increases from 850 m/s to 1100 m/s (i.e., a 250-m/s speed increment), which is presented by the color change from green to yellow in the cross-section. The V_{SV} speeds steadily increase from 1100 m/s to 1200 m/s in the depth range 30-40 m for which the inverted speeds show a structure more like a one-layer, which is depicted by the red color in the color scale. Such deeper structures are solved by the longer period Rayleigh surface waves (FM), which exhibit lower resolution power in the vertical direction.

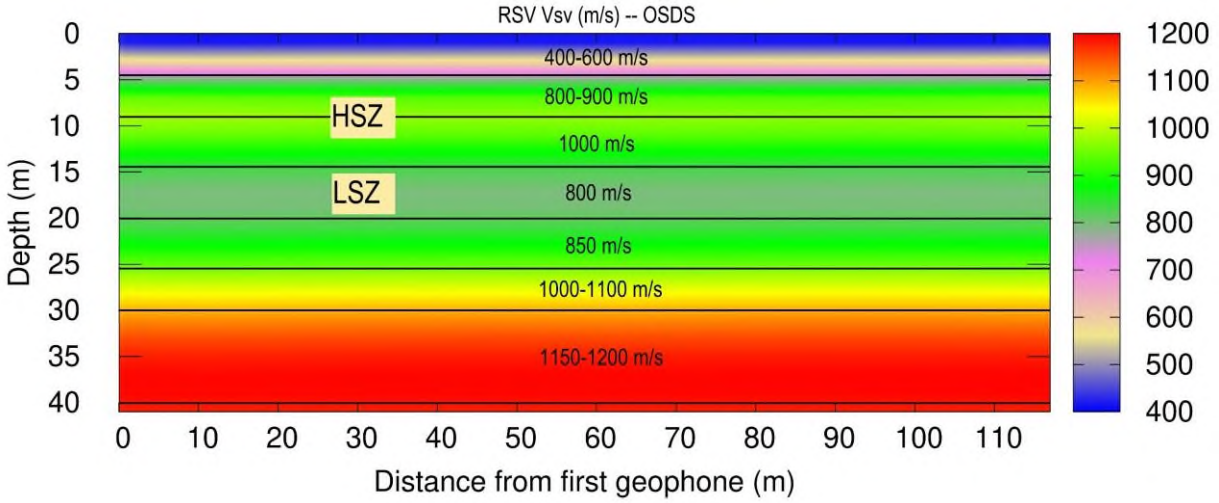

Figure 11: Two-dimensional (2D) vertical cut corresponding to the shear-wave (V_{SV}) speeds obtained by the inversion of group and phase speed dispersion curves is shown. The one-station (OS) and double-station (DS) approaches are joined.

4. DISCUSSION AND CONCLUSIONS

We mathematically replicate the Rayleigh surface waves in a multilayered subsurface. The vertical component synthetic seismograms are calculated to characterize the wave propagation. These synthetic calculations are utilized to evaluate the performance of the programmed technique proposed for the determination of the seismic speed structure above 40-m depth. The data collection geometry is assumed as the CSG, which employs multiple stations aligned along a linear line to record the Rayleigh surface vibrations. The CSG is employed to estimate the 2D variation of vertically polarized shear-vibration (V_{SV}) speeds with depth. In the programmed approach, we first estimate the average structure beneath the geophone spread for which the weighted preconditioned linear radon transform (WPLRT) is employed to solve the phase speeds. Secondly, the OS group speeds are realized by applying the multiple filter technique (MFT) to each geophone recording. In the third step, we calculate the cross-correlations between two stations in the CSG. Herein, the cross-correlograms, which are free of the source phase, are employed to acquire the DS group and phase speeds. The WPLRT approach utilizing the phase speeds provides an initial model, which effectively represents the 1D V_{SV} speeds under the CSG, which is discretized using a set of grid points (Figure 1). This initial model is then used to invert the OS (group speeds) and DS (phase and group speeds) data. In this way, the subsurface beneath each grid point is represented by an individual 1D V_{SV} depth profile and then these profiles are joined to build the 2D vertical cut under the CSG.

In Table 2, we compare the current algorithm with similar studies, i.e., CMP-CC MASW [47, 48, 49, 50, 51] and CMP-CC SPAC [52, 53, 54, 55, 56] where CMP stands for Common Midpoint and CC for Cross-Correlation. The CMP-CC [57] is a procedure utilized to maximize the spatial resolution of MASW or SPAC. The CMP-CC MASW involves multi-channel and multi-shot surface waves [57] in which continuous distance profiling is performed to collect horizontally extended surface wave data. There exist common midpoints between pairs of receivers in a common shot gather for which cross-correlations are computed. The latter procedure is repeated for multi-shot surface waves. Those correlation signals sharing the same CMP and receiver spacing are stacked from which CMP-CC gathers are eventually constructed. The conventional MASW method [11] is applied to the CMP-CC gathers to compute the phase velocities, which are then inverted to attain a pseudo 2D V_{SV} structure underneath the studied area [57]. The CMP-CC SPAC, which is a multi-channel passive surface wave method, works in an analogous way to that in the CMP-CC MASW. Several minutes of ambient noise is recorded for spatial autocorrelation (SPAC) analysis. The 2D receiver array is divided into several blocks and for each

receiver pair in each block, SPAC traces (i.e., coherencies) are computed [24]. In the frequency domain, computed coherencies over all blocks are averaged and those coherencies sharing the same common midpoint are grouped as CMP-SPAC gathers. The observed coherences are compared with the theoretical Bessel function to calculate the phase velocities, which are finally inverted to reconstruct a pseudo 2D/3D V_{SV} model underneath the region of interest [58].

Table 2: Brief comparison of the current algorithm with the CMP-CC MASW and CMP-CC SPAC methods.

Properties	Current study	CMP-CC MASW	CMP-CC SPAC
Active/Passive Source	Active	Active	Passive
Dispersion curves	Phase and Group Velocity	Commonly Phase Velocity	Commonly Phase Velocity
Resolution depth (m)	Shallow (< 50 m)	Shallow (< 50 m)	Deep (> 50 m)
2D/3D Tomographic imaging	Yes	Yes	Yes

Concluding remarks

- The phase velocities are computed from the phase spectrum of surface waves while the amplitude spectrum is utilized to calculate the group velocities. We jointly invert group and phase velocities to predict the near-surface shear-wave velocities (V_{SV}).
- The current algorithm involves hundreds of dispersion curves (both phase and group velocity). To hand-pick this much dispersion curve can be quickly overwhelming. We select these dispersion curves by employing a programmed scheme like the one reported in Çakır and Kutlu (2023) [32].
- The phase velocities at low frequencies are determined by using a long receiver array for which a strong seismic source (e.g., a shaker or vibrator) is needed to deliver the surface wave energy up to the end of profile.
- The parameter $N_c = 30$, which is the minimum number of geophone intervals between two stations can be set to 20 or 10, which will help increase the number of DS dispersion data along with an increment in the lateral resolution.
- An observed dispersion curve is converted into a dispersion curve defined at a grid point for which a linear system regularized around a reference slowness computed from the average of the observed slowness is solved along with a damping parameter.
- Like the CMP-CC MASW and CMP-CC SPAC methods, the current algorithm can predict the 2D variation of V_{SV} underneath the 2D continuous-profiling and this coverage can be extended into a 3D tomographic study along with the 2D cross-profiling.

Declaration of Ethical Standards

The authors of this article declare that the materials and methods used in this study do not require ethical committee permission and/or legal-special permission.

Credit Authorship Contribution Statement

CRediT (Contributor Roles Taxonomy) was introduced with the intention of recognizing individual author contributions, reducing authorship disputes, and facilitating collaboration.

Declaration of Competing Interest

The authors declare that they have no known competing financial interests or personal relationships that could have appeared to influence the work reported in this paper.

Funding / Acknowledgements

We are grateful to the anonymous reviewers for critically reviewing the manuscript.

Data Availability

There is not any data from a data repository.

5. REFERENCES

[1] D.A. Robinson, A. Binley, N. Crook, F.D. Day-Lewis, T.P.A. Ferre, V.J.S. Grauch, R. Knight, M. Knoll, V. Lakshmi, R. Miller, J. Nyquist, L. Pelleri, K. Singha, and L. Slater, "Advancing process-based watershed hydrological research using near-surface geophysics: a vision for, and review of, electrical and magnetic geophysical methods," *Hydrological Processes*, vol. 22, pp. 3604–3635, 2008.

[2] L.V. Socco, and C. Strobbia, "Surface-wave method for near-surface characterization: a tutorial," *Near Surface Geophysics*, vol. 2, pp. 165–185, 2004.

[3] V. Pérez-Gracia, J.O. Caselles, J. Clapes, R. Osorio, G. Martínez, and J.A. Canas, "Integrated near-surface geophysical survey of the Cathedral of Mallorca," *Journal of Archaeological Science*, vol. *36*, pp. 1289–1299, 2009.

[4] Y. Huang, and M. Yu, *Hazard analysis of seismic soil liquefaction*. Springer, Singapore, 2017.

[5] V. Balaram, "Rare earth elements: a review of applications, occurrence, exploration, analysis, recycling, and environmental impact," *Geoscience Frontiers*, vol. 10, pp. 1285–1303, 2019.

[6] C. Lin, X. Wang, L. Nie, H. Sun, Z. Xu, Y. Du, and L. Liu, "Comprehensive geophysical investigation and analysis of lining leakage for water-rich rock tunnels: a case study of Kaiyuan Tunnel, Jinan, China," *Geotechnical and Geological Engineering*, vol. 38, pp. 3449–3468, 2020.

[7] E.A. Ayolabi, A.F. Folorunso, and O.T. Kayode, "Integrated methods for environmental Assessment of municipal dumpsite system," *International Journal of Geosciences*, vol. 4, pp. 850–862, 2013.

[8] M. Everett, *Near-surface applied geophysics*. Cambridge University Press, 2013.

[9] A. Turesson, "A comparison of methods for the analysis of compressional, shear, and surface wave seismic data, and determination of the shear modulus," *Journal of Applied Geophysics*, vol. 61, pp. 83–91, 2007.

[10] K. Luxbacher, E. Westman, P. Swanson, and M. Karfakis, "Three-dimensional time-lapse velocity tomography of an underground longwall panel," *International Journal of Rock Mechanics and Mining Sciences*, vol. 45, pp. 478–485, 2008.

[11] C.B. Park, R.D. Miller, and J. Xia, "Multichannel analysis of surface waves," *Geophysics*, vol. 64, pp. 800808, 1999.

[12] A. Ali, M. Ullah, A. Barkat, W.A. Raza, and A. Qadir, "Multi-channel analysis of surface waves (MASW) using dispersion and iterative inversion techniques: implications for cavity detection and geotechnical site investigation," *Bulletin of Engineering Geology and the Environment*, vol. 80, pp. 9217–9235, 2021.

[13] G. Dal Moro, "MASW? A critical perspective on problems and opportunities in surface-wave analysis from active and passive data (with few legal considerations)," *Physics and Chemistry of the Earth*, vol. 130, pp. 103369, 2023.

[14] H. Nakahara, K. Emoto, and T. Nishimura, "Extending the formulation of the spatial autocorrelation (SPAC) method to strain, rotation and tilt," *Geophysical Journal International*, vol. 227, pp. 287–302, 2021

[15] C. Feng, K. Yamaoka, R. Ikuta, T. Watanabe, and S. Tsuji, "Surface wave monitoring using ambient noise for detecting temporal variations in underground structures in landslide area," *Engineering Geology*, vol. 341, pp. 107706, 2024.

[16] Q. Liu, L. Lu, K. Wang, L. Chang, and Y. Zhu, "Rayleigh Wave Phase Velocity Maps at Regional Scale Inferring from SPAC of Ambient Noise at a Dense Array: A Case Study in Northeastern

Tibetan Plateau," *Pure and Applied Geophysics*, vol. 180, pp. 1973–1988, 2023.
[17] S. Coccia, V. Del Gaudio, N. Venisti, and J. Wasowski, "Application of Refraction Microtremor (ReMi) technique for determination of 1-D shear wave velocity in a landslide area," *Journal of Applied Geophysics*, vol. 71, pp. 71–89, 2010.
[18] J.N. Louie, A. Pancha, and B. Kissane, "Guidelines and pitfalls of refraction microtremor surveys," *Journal of Seismology*, vol. 26, pp. 567–582, 2022.
[19] K. Aki, "Space and time spectra of stationary stochastic waves, with special reference to microseisms," *Bulletin of the Earthquake Research Institute*, vol. 35, pp. 415–456, 1957.
[20] T.F. Abdallatif, A.A. Khozyma, and A.A. Ghandour, "Determination of Seismic Site Class and Potential Geologic Hazards using Multi-Channel Analysis of Surface Waves (MASW) at the Industrial City of Abu Dhabi, UAE," *Journal of Astronomy and Geophysics*, vol. 11, pp. 193–209, 2022.
[21] B. Mi, J. Xia, J.H. Bradford, and C. Shen, "Estimating Near-Surface Shear-Wave-Velocity Structures Via Multichannel Analysis of Rayleigh and Love Waves: An Experiment at the Boise Hydrogeophysical Research Site," *Surveys in Geophysics*, vol. 41, pp. 323–341, 2020.
[22] K. Zheng, W. Hou, J. Li, J. Yang, Y. Yang, F. Xiao, and Y. Chen, "Imaging urban near-surface structure with passive surface waves method: A case study in Guangzhou, southern China," *Journal of Applied Geophysics*, vol. 215, pp. 105089, 2023.
[23] M. Asten, A. Askan, and S. Karimzadeh, "Blind study site assessment of shear-wave velocity at Kumamoto City, Japan, using direct-fitting SPAC methods," *Earth, Planets and Space*, vol. 75, pp. 40, 2023.
[24] Q. Liu, L. Lu, T. Qin, and L. Chang, "Determination of surface-wave phase velocities by zeros of Aki's spectrum of active-source records. Application to the dense array in Tongzhou, China," *Earthquake Science*, vol. 38, pp. 1–16, 2024.
[25] K. Abdelrahman, A.B. Saadon, and S. Qaysi, "Estimating shear wave velocity and site characterization of western Riyadh City, Saudi Arabia based on multichannel analysis of surface waves," *Frontiers in Earth Science*, vol. 12, pp. 1395431, 2024.
[26] A. Kaviani, A. Paul, A. Moradi, P.M. Mai, S. Pilia, L. Boschi, G. Rümpker, Y. Lu, Z. Tang, and E. Sandvol, "Crustal and uppermost mantle shear wave velocity structure beneath the Middle East from surface wave tomography," *Geophysical Journal International*, vol. 221, pp. 1349–1365, 2020.
[27] Z. Zhang, H. Yao, and Y. Yang, "Shear wave velocity structure of the crust and upper mantle in Southeastern Tibet and its geodynamic implications," *Science China Earth Sciences*, vol. 63, pp. 1278–1293, 2020.
[28] K.A. Berteussen, "Moho depth determinations based on spectral analysis of NORSAR long period P waves," *Physics of the Earth and Planetary Interiors*, vol. 15, pp. 13–27, 1977.
[29] R.B. Herrmann, *Computer programs in seismology, version 3.30*. St. Louis University, Missouri, United States, 2002.
[30] Y. Luo, J. Xia, R.D. Miller, Y. Xu, J. Liu, and Q. Liu, "Rayleigh-wave mode separation by high-resolution linear radon transform," *Geophysical Journal International*, vol. 179, pp. 254–264, 2009.
[31] A. Dziewonski, S. Bloch, and M. Landisman, "A technique for the analysis of transient seismic signals," *Bulletin of Seismological Society of America*, vol. 59, pp. 427–444, 1969.
[32] Ö. Çakır, and Y.A. Kutlu, "A New Method for Selecting the Phase and Group Velocity Dispersion Curves of Rayleigh and Love Surface Waves: Real Data Case of Central Anatolia, Turkey (Türkiye)," *Indonesian Journal of Earth Sciences*, vol. 3, pp. 795, 2023.
[33] L. Gao, J. Xia, Y. Pan, and Y. Xu, "Reason and Condition for Mode Kissing in MASW Method," *Pure and Applied Geophysics*, vol. 173, pp. 1627–1638, 2016.
[34] Ö. Çakır, and N. Coşkun, "Theoretical Issues with Rayleigh Surface Waves and Geoelectrical Method Used for the Inversion of Near Surface Geophysical Structure," *Journal of Human, Earth, Future*, vol. 2, pp. 183–199, 2021.
[35] D.J. Zywicki, and G.J. Rix, "Mitigation of Near-Field Effects for Seismic Surface Wave Velocity Estimation with Cylindrical Beamformers," *Journal of Geotechnical and Geoenvironmental Engineering*,

vol. 131, pp. 970–977, 2005.
[36] A. Tarantola, "Linearized inversion of seismic reflection data," *Geophysical Prospecting*, vol. 32, pp. 998–10115, 1984.
[37] R.J. Geller, and T. Hara, "Two efficient algorithms for iterative linearized inversion of seismic waveform data," *Geophysical Journal International*, vol. 115, pp. 699–710, 1993.
[38] Ö. Çakır, "Seismic crust structure beneath the Aegean region in southwest Turkey from radial anisotropic inversion of Rayleigh and Love surface waves," *Acta Geophysica*, vol. 66, pp. 1303–1340, 2018.
[39] Ö. Çakır, "Love and Rayleigh Waves Inverted for Vertical Transverse Isotropic Crust Structure beneath the Biga Peninsula and the surrounding area in NW TURKEY," *Geophysical Journal International*, vol. 216, pp. 2081–2105, 2019.
[40] Ö. Çakır, "The multilevel fast multipole method for forward modelling the multiply scattered seismic surface waves," *Geophysical Journal International*, vol. 167, pp. 663-678, 2006.
[41] I.B. Morozov, and M. Din, "Use of receiver functions in wide-angle controlled-source crustal data sets," *Geophysical Journal International*, vol. 173, pp. 299–308, 2008.
[42] V. Maupin, "Upper-mantle structure in southern Norway from beamforming of Rayleigh wave data presenting multipathing," *Geophysical Journal International*, vol. 185, pp. 985–1002, 2011.
[43] Ö. Çakır, "A multilevel fast multipole method to compute propagation of multiply scattered 2.5-D teleseismic surface waves underneath a linear or quasi-linear seismic station array," *International Journal of Physical Sciences*, vol. 7, pp. 5687–5700, 2012.
[44] J. Julià, C.J. Ammon, R.B. Herrmann, and A.M. Correig, "Joint inversion of receiver function and surface wave dispersion observations," *Geophysical Journal International*, vol. 143, pp. 99–112, 2000.
[45] Ö. Çakır, and N. Coşkun, "Love Surface Waves and Electrical Resistivity Used to Delineate the Near Surface Geophysical Structure: Theoretical Considerations," *Earth Sciences Malaysia*, vol. 5, pp. 104–113, 2021.
[46] Ö. Çakır, and N. Coşkun, "Dispersion of Rayleigh Surface Waves and Electrical Resistivities Utilized to Invert Near Surface Structural Heterogeneities," *Journal of Human, Earth, Future*, vol. 3, pp. 1–16, 2022.
[47] P.P. Kruiver, M. Pefkos, E. Meijles, G. Aalbersberg, X. Campman, W. van der Veen, A. Martin, K. Ooms-Asshoff, J. J. Bommer, A. Rodriguez-Marek, R. Pinho, H. Crowley, F. Cavalieri, A.A. Correia, and J. van Elk, "Incorporating dwelling mounds into induced seismic risk analysis for the Groningen gas field in the Netherlands," *Bulletin of Earthquake Engineering*, vol. 20, pp. 255–285, 2022.
[48] K. Leontarakis, C. Orfanos, and G. Apostolopoulos, "Common-midpoint cross-correlation stacking tomography: A 3D approach for frequency-dependent mapping of Rayleigh waves, group and phase velocity throughout an active seismic network," *Near Surface Geophysics*, vol. 21, pp. 39–64, 2023.
[49] I. Barone, J. Boaga, A. Carrera, A. Flores-Orozco, and G. Cassiani, "Tackling Lateral Variability Using Surface Waves: A Tomography-Like Approach," *Surveys in Geophysics*, vol. 42, pp. 317–338, 2021.
[50] F. Cheng, J. Xia, C. Shen, Y. Hu, Z. Xu, and B. Mi, "Imposing Active Sources during High-Frequency Passive Surface-Wave Measurement," *Engineering*, vol. 4, pp. 685–693, 2018.
[51] B. Mi, J. Xia, J.H. Bradford, and C. Shen, "Estimating Near-Surface Shear-Wave-Velocity Structures Via Multichannel Analysis of Rayleigh and Love Waves: An Experiment at the Boise Hydrogeophysical Research Site," *Surveys in Geophysics*, vol. 41, pp. 323–341, 2020.
[52] M.S. Craig, K. Hayashi, and Ö. Kozacı, "Active and passive seismic surface wave methods for levee assessment in the Sacramento–San Joaquin Delta, California, USA," *Near Surface Geophysics*, vol. 19, pp. 141–154, 2021.
[53] J. Pang, J. Xia, C. Zhou, X. Chen, F. Cheng, and H. Xing, "Common-midpoint two-station analysis of estimating phase velocity using high-frequency ambient noise," *Soil Dynamics and Earthquake*

Engineering, vol. 159, pp. 107356, 2022.

[54] K. Hayashi, M.W. Asten, W.J. Stephenson, C. Cornou, M. Hobiger, M. Pilz, and H. Yamanaka, "Microtremor array method using spatial autocorrelation analysis of Rayleigh-wave data," *Journal of Seismology*, vol. 26, pp. 601–627, 2022.

[55] F.J. Chávez-García, M.V. Manakou, F. Hollender, and D.G. Raptakis, "Site effects using methods based on lateral homogeneity and laterally heterogeneous media: An impossible marriage?," *Bulletin of Earthquake Engineering*, vol. 16, pp. 2729–2756, 2018.

[56] F. Cheng, J. Xia, Z. Xu, Y. Hu, and B. Mi, "Frequency–Wavenumber (FK)-Based Data Selection in High-Frequency Passive Surface Wave Survey," *Surveys in Geophysics*, vol. 39, pp. 661–682, 2018.

[57] K. Hayashi, and H. Suzuki, "CMP cross-correlation analysis of multi-channel surface-wave data," *Exploration Geophysics*, vol. 35, pp. 7–13, 2004.

[58] K. Hayashi, J.M. Lorenzo, and A. Gostic, "Application of 2D ambient noise tomography to levee safety assessment in New Orleans," *The Leading Edge*, vol. 37, pp. 740–745, 2018.